Ocean Engineering 278 (2023) 114594

Contents lists available at ScienceDirect

Ocean Engineering

journal homepage: www.elsevier.com/locate/oceaneng

Reliability analysis of floating wind turbine dynamic cables under realistic environmental loads

Salem Okpokparoro [a,b], Srinivas Sriramula [a,*]

[a] University of Aberdeen, Aberdeen, AB24 3UE, United Kingdom
[b] Offshore Renewable Energy Catapult, Offshore House, Albert Street, Blyth, Northumberland, NE24 1LZ, United Kingdom

ARTICLE INFO

Keywords:
Dynamic power cable
Reliability analysis
Floating wind turbine
Analytical model
Fatigue damage
Site-specific reliability assessment

ABSTRACT

The need for more robust design of dynamic cables used for power export in floating wind turbine (FWT) systems is accentuated by the frequent occurrence of power cable failures. Such failures contribute considerably to the cost of global offshore wind farm losses. Fatigue is often times a critical consideration in the structural safety of these cables. This is understandably so, given that they experience numerous loading cycles–mainly induced by the combined action of wind and waves throughout their service life. It is therefore pertinent that the reliability level attainable by these cables is quantified and elaborated upon. In this paper, a probabilistic reliability analysis approach is developed to quantify the reliability levels of dynamic power cables. Uncertainties emanating from the randomness of realistic environmental scatter, geometric and material variables are all taken into account in this study. To facilitate the computation of the structural demands on the dynamic power cable, an efficient analytical model was developed. Key aspects such as cable–soil interaction and boundary-layer phenomenon are captured by the analytical model. Kriging metamodel is then employed to propagate relevant uncertainties into the reliability problem, making it possible to quantify the reliability levels of these cables.

1. Introduction

Floating offshore wind no doubt is very much in its infancy. Nevertheless, it is largely viewed as the key to unlocking the largely untapped rich wind resources available in deep waters. However, with floating systems comes peculiar challenges, especially considering their increased compliance to environmental loads. Power export cables for these systems are therefore more susceptible to failures. Such failures can be very costly, in terms of grid losses and incurred costs of maintenance and repairs. It was reported by GCube Insurance—a leading renewable energy underwriter, that in a 12 month period, offshore cabling failures accounted for 55% of overall claims they handled and around 75% of total claim value (GCube Insurance, 2019). Improving the design of dynamic power cables for floating wind turbines (FWTs) is crucial in curbing cabling failures. This was one of the key findings of Stage II Phase II report (The Carbon Trust, 2020b) of the collaborative research and development initiative piloted by The Carbon Trust–the Floating Wind Joint Industry Project, FWJIP (The Carbon Trust, 2020a). Integral to achieving such improved design is the accurate quantification and improvement of the structural reliability of these cables. This forms the main motivation for the work done in this paper.

For floating structures, dynamic power cables are a favoured choice when compared to the simple free hanging catenary configurations. They have been shown to perform better than simple free hanging configurations owing to their decoupling of platform motions (Thies et al., 2012; Rentschler et al., 2020). Several works on analytical models for load prediction for pipelines/cables used for offshore oil and gas applications published in Refs. such as Lenci and Callegari (2005), Quéau et al. (2013), Wang et al. (2019, 2012), to mention but a few. There is very limited work in regard to FWT applications. The dynamic response of a FWT dynamic power cable can be different to a riser in oil and gas applications because offshore platforms are devoid of the influence of an actively rotating rotor and control system on their motion response. However, for FWTs, such aspects can significantly contribute to platform motions and the resulting loading regimes. Also, the internal fluid flowing through risers and the associated temperature can significantly impact their dynamic response (Vásquez and Avila, 2019)—this is not the case for a dynamic power cable attached to a FWT. Sobhaniasl et al. (2020), Rentschler et al. (2019, 2020), Thies et al. (2012) are the few examples of studies on dynamic power cables for FWT systems. Sobhaniasl et al. (2020) carried out fatigue analysis of a FWT power cable by applying the time history of the total rotor aerodynamic load outputted from the numerical code, FAST (Jonkman and Jonkman, 2016) to an ANSYS AQWA model where the hydrodynamics

* Corresponding author.
E-mail address: s.sriramula@abdn.ac.uk (S. Sriramula).

https://doi.org/10.1016/j.oceaneng.2023.114594
Received 6 February 2023; Received in revised form 29 March 2023; Accepted 13 April 2023
Available online 27 April 2023

and power cable were modelled. This approach neglects the influence of the turbine controllers on the structural dynamics of the coupled wind turbine system. Also, the proprietary software for marine dynamics modelling, OrcaFlex® has been used for power cable analysis by authors such as Rentschler et al. (2019, 2020), Thies et al. (2012). Use of high-fidelity finite element models can be computationally challenging when evaluation of the loading regimes for numerous combinations of environmental states and/or cable configurations is required. It is therefore imperative to have simplified models capable of quick and accurate prediction of the loads acting on the power cable—making it possible to assess structural reliability and speeding up concept selection. A detailed analysis can then be performed in the final design stage. Widely used medium-fidelity aero-hydro-servo-elastic codes such as OpenFAST (Jonkman and Jonkman, 2016), HAWC2 (DTU, 2021) and Bladed (Bossanyi, 2015) do not currently allow the addition of non-structural components such as dynamic power cables. To this end, an analytical model capable of predicting the loads on the power cable given time series of platform motions was developed in this paper. The developed analytical model is fast and efficient—suitable for carrying out thousands of load evaluations typically required for probabilistic reliability analysis.

Key aspects in the formulation of the analytical model in this paper can be found in Lenci and Callegari (2005), Quéau et al. (2013), Wang et al. (2019, 2012). In these works, the part of the cable resting on the seabed was considered infinite and the hang-off angle could be measured before hand. In our study, the touchdown section of the cable is bounded by a finite interval and the hang-off angle is an unknown parameter to be computed. The developed model is capable of capturing key aspects such as cable–soil interaction and the boundary-layer phenomenon that occurs close to the touchdown point (TDP). The boundary-layer phenomenon is captured by ensuring the continuity of shear and bending moment at the TDP via the relaxation of the rigidity of the seabed and modelling the cable in the boundary-layer region as a beam that supports flexure (Lenci and Callegari, 2005). Comparisons with finite element model presented in this paper indicates that the effect of bending stiffness in the boundary-layer region is not negligible.

Estimating the fatigue life of FWT' dynamic cables is a complex and nontrivial endeavour. Numerous time domain simulations are required to effectively capture the variability of the environmental conditions at the site the wind turbine would operate throughout its design life. In general, the enormity of the computational cost of evaluating the dynamic responses and resulting fatigue damage of Offshore Wind Turbine (OWT) components is largely attributable to the number of time domain simulations required. The number of simulations required can be more than 50,000 (Vorpahl et al., 2013; Murcia et al., 2018). Surrogate models are gaining attention in the design of FWTs. Surrogate models, also referred to as metamodels, are created by constructing a mapping of a relatively few sample points generated from the uncertain input variables to their corresponding FWT responses that are calculated by running the original computationally expensive model. By so doing, the original complex model can then be effectively replaced by the constructed transfer function (Wilkie and Galasso, 2021). Several surrogate techniques have been employed by researchers for predicting the nonlinear behaviour of the wind turbine using limited number of appropriately chosen sample points, such as: Gaussian process modelling (Kriging) (Li and Zhang, 2020; Okpokparoro and Sriramula, 2021; Wilkie and Galasso, 2021; Morató et al., 2019; Stieng and Muskulus, 2020; Yang et al., 2015), response surface model (Toft et al., 2016; Murcia et al., 2018), polynomial chaos expansion (Murcia et al., 2018; Stieng and Muskulus, 2020) and machine learning techniques. In this paper, Kriging model is employed for mapping the input random variables to the short term fatigue damage along selected points on the dynamic cable. Reliability analysis is then performed by formulating appropriate limit state function (LSF) and employing first-order reliability method (FORM) and second-order reliability method (SORM) to obtain the failure probability and reliability index of the dynamic power cable. At the time of writing this paper, no work has attempted to assess the reliability levels of FWT export power cables. The analysis conducted in this paper bridges this gap in knowledge. The reliability framework proposed in this paper only considered fatigue damage under normal turbine operating conditions described by IEC 61400-3 (IEC, 2019) design load case (DLC) 1.2. A great proportion of the turbine life is spent in this DLC scenario. Also, dynamic cables are more susceptible to failure due to fatigue compared to ultimate loads. However, the methods proposed in this work can be extended to analyse for extreme conditions. This will be covered in a further study.

2. Computational tools and analytical model development

2.1. Dynamic simulations

The aero-hydro-servo-elastic solver, OpenFAST (Jonkman and Jonkman, 2016) is used to output time series of platform displacements and rotations which serve as inputs to the analytical model. The FWT model used for the analysis is the National Renewable Energy Laboratory's (NREL's) 5-MW baseline offshore turbine mounted on the OC3-Hywind spar buoy (Jonkman, 2010). The NREL code, TurbSim (Jonkman and Buhl, 2006) is employed for the generation of full-field random turbulent wind files needed for each time domain simulation. Given that the wind file needed at the execution of a OpenFAST simulation has to be stored in memory, repeated periodic 10-min long wind files were used to circumvent the huge memory requirements where 1-hr long simulations are performed in this study. A MATLAB program is developed for the implementation of the analytical model of the dynamic power cable.

2.2. Fundamental assumptions of the analytical model

To achieve a computationally efficient implementation with negligible effect on accuracy, the following assumptions were made:

1. Three-dimensional (3D) out-of-plane effects are neglected as the analytical model is a planar formulation.
2. The seabed is considered to be horizontal, flat and the effect of seabed friction is ignored.
3. The contribution of the power cable to the structural dynamics of the FWT system is considered to be negligible, hence a decoupled analysis can be employed. Results presented in Section 3 show that this assumption is valid.
4. To simplify the formulation of the analytical model, the axial deformation of the power cable is neglected. This does not affect the validity of the model as the axial stiffness has meagre influence in practical applications.
5. Although hydrodynamic loads including sea current loads are computed for sub-structural elements of the FWT in OpenFAST, the analytical model does not consider hydrodynamic loads acting on the cable.
6. The boundary-layer phenomenon close to the point where the power cable is attached to the platform as well as at the hog and sag bends are not considered. Comparison with an FE model developed in OrcaFlex showed negligible disparity.

The present study's focus on the development of a fundamental framework for computationally efficient reliability analysis options necessitated the highlighted assumptions. The proposed analytical model for predicting the mechanical characteristics of these cables is an initial step in this direction.

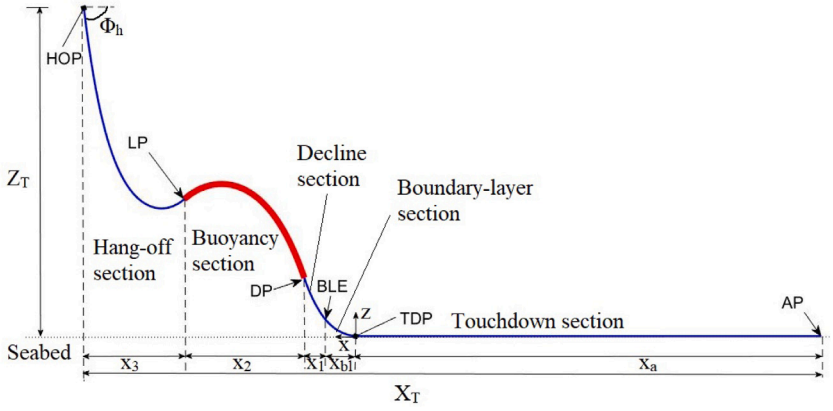

Fig. 1. Schematic representation of the 2D planar model.

2.3. Governing equations

The equations discussed in this section describe the set up of a 2D planar system for the computation of the configuration and mechanical properties of the lazy-wave dynamic power cable. The transformation from the 3D system to the 2D planar system is described in Section 2.4. The 2D planar system is shown in Fig. 1. The global coordinate system of the planar model (X, Z) is set up such that its origin is at the touchdown point (TDP) of the cable with the X-axis increasing from the TDP to the point where the power cable is attached to the floating platform (called the hang-off point (HOP)) and Z-axis points vertically upwards. At the HOP, the cable forms an inclination angle Φ_h with the horizontal. From the HOP to the lift point (LP) is the hang-off section, with a horizontal span x_3. The buoyancy modules are installed on the cable section bounded by the LP and the drag point (DP) with a horizontal span x_2–defining the buoyancy section. From the DP to the boundary-layer end (BLE) is the decline section with horizontal span of x_1. The boundary-layer section is from the BLE to the TDP with a horizontal distance of x_{bl}. The section of the cable resting on the seabed is called the touchdown section. The horizontal distance for this section is x_a–distance from the TDP to an anchorage point (AP).

2.3.1. Catenary segment

The catenary segment comprises three parts: the hang-off section (HOS), the buoyancy section (BS) and the decline section (DS). Each of these suspended catenary-shaped sections are modelled as beams with their bending stiffness neglected such that only axial tension is supported (Lenci and Callegari, 2005; Villaggio, 1997).

The governing equation of the catenary segment is given by Eq. (1).

$$z''(x) = \delta\sqrt{1+[z'(x)]^2}, \quad (x_{bl}) \le x \le (x_3+x_2+x_1+x_{bl}) \tag{1}$$

where $\delta = P/T_H$, P is the submerged weight per unit length of the cable and T_H is the constant horizontal component of the tension T. Eq. (2) gives the slope angle, curvature, and tension respectively.

$$\Phi(x) = \arctan([z'(x)]); \quad \kappa(x) = \frac{\delta^3}{[z''(x)]^2}; \quad \tilde{T}(x) = \frac{P}{\delta^2}z''(x) \tag{2}$$

The general solution to Eq. (1) for the hang-off section, buoyancy section and the decline section are given by Eq. (3), (4) and (5) respectively.

$$z_{hos}(x) = c_1 + \frac{1}{\delta_1}\cosh(\delta_1 x + c_2), \quad (x_2+x_1+x_{bl}) \le x \le (x_3+x_2+x_1+x_{bl}) \tag{3}$$

$$z_{bs}(x) = c_3 + \frac{1}{\delta_2}\cosh(\delta_2 x + c_4), \quad (x_1+x_{bl}) \le x \le (x_2+x_1+x_{bl}) \tag{4}$$

$$z_{ds}(x) = c_5 + \frac{1}{\delta_3}\cosh(\delta_3 x + c_6), \quad (x_{bl}) \le x \le (x_1+x_{bl}) \tag{5}$$

where x_1–x_3, x_{bl}, δ_1–δ_3 and c_1–c_6 are unknowns. Given that the catenary cable does not support flexure, the bending moment ($\tilde{M}$) is approximated as the product of bending stiffness EI and curvature κ while shear ($\tilde{S}$) is approximated as the differentiation of the bending moment as shown in the following equations:

$$\tilde{M}(x) = \frac{EI\delta^3}{[z''(x)]^2}; \quad \tilde{S}(x) = \frac{d\tilde{M}}{ds} = \frac{d\tilde{M}}{dx}\frac{dx}{ds} \tag{6}$$

where s is the arc length. To further evaluate the expression for shear, consider that $ds^2 = dx^2 + dz^2$. This gives $dx/ds = (1+[z'(x)]^2)^{-\frac{1}{2}}$. We can then obtain the shear as: $\tilde{S}(x) = -2EI\delta^6[z'(x)][z''(x)]^{-4}$. Thus, the bending moment, shear and tension for the three sections are given as follows:

$$\tilde{M}_{hos}(x) = \frac{EI\delta_1^3}{[z''_{hos}(x)]^2}, \quad (x_2+x_1+x_{bl}) \le x \le (x_3+x_2+x_1+x_{bl}) \tag{7}$$

$$\tilde{M}_{bs}(x) = \frac{EI\delta_2^3}{[z''_{bs}(x)]^2}, \quad (x_1+x_{bl}) \le x \le (x_2+x_1+x_{bl}) \tag{8}$$

$$\tilde{M}_{ds}(x) = \frac{EI\delta_3^3}{[z''_{ds}(x)]^2}, \quad (x_{bl}) \le x \le (x_1+x_{bl}) \tag{9}$$

$$\tilde{S}_{hos}(x) = -2EI\delta_1^6\frac{z'_{hos}(x)}{[z''_{hos}(x)]^4}, \quad (x_2+x_1+x_{bl}) \le x \le (x_3+x_2+x_1+x_{bl}) \tag{10}$$

$$\tilde{S}_{bs}(x) = -2EI\delta_2^6\frac{z'_{bs}(x)}{[z''_{bs}(x)]^4}, \quad (x_1+x_{bl}) \le x \le (x_2+x_1+x_{bl}) \tag{11}$$

$$\tilde{S}_{ds}(x) = -2EI\delta_3^6\frac{z'_{ds}(x)}{[z''_{ds}(x)]^4}, \quad (x_{bl}) \le x \le (x_1+x_{bl}) \tag{12}$$

$$\tilde{T}_{hos}(x) = \frac{P}{\delta_1^2}z''_{hos}(x), \quad (x_2+x_1+x_{bl}) \le x \le (x_3+x_2+x_1+x_{bl}) \tag{13}$$

$$\tilde{T}_{bs}(x) = \frac{P_b}{\delta_2^2}z''_{bs}(x), \quad (x_1+x_{bl}) \le x \le (x_2+x_1+x_{bl}) \tag{14}$$

$$\tilde{T}_{ds}(x) = \frac{P}{\delta_3^2}z''_{ds}(x), \quad (x_{bl}) \le x \le (x_1+x_{bl}) \tag{15}$$

For the three sections, the equivalent bending stiffness EI is taken as the same value. The submerged weight of the buoyancy section P_b points vertically upwards while the hang-off catenary and decline section all have the same submerged weight P which acts vertically downwards.

2.3.2. Boundary-layer section

The Boundary-layer section is the section located between the TDP and the drag point (DP) which spans an unknown interval x_{bl} such that the inclination slope is small. The tension T_{bl} for this section is assumed constant as the change in tension can be neglected (Croll, 2000). Within the interval x_{bl}, the boundary phenomenon is significant

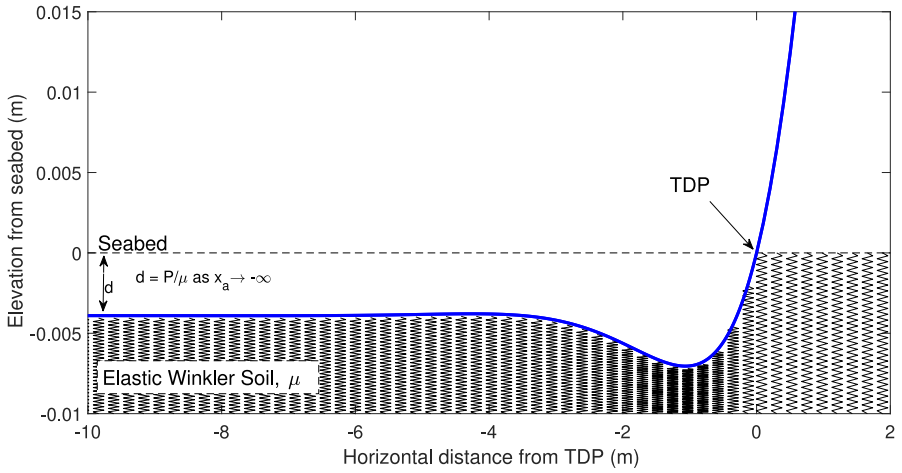

Fig. 2. Zoom around the touchdown zone.

hence the linear deformation beam theory is used in order to ensure the continuity of bending moment and shear at TDP—taking into account the influence of the cable's bending stiffness. The governing equation for the boundary-layer section is derived as:

$$EIz''''_{bl}(x) - T_{bl}z''_{bl}(x) = P, \quad 0 \le x \le x_{bl} \tag{16}$$

The general solution of Eq. (16) is given by Eq. (17) while the bending moment and shear for the boundary-layer section are computed according to Eq. (18) and (19) respectively.

$$z_{bl}(x) = -\frac{P}{2T_{bl}}x^2 + c_7 + c_8 x + c_9 \sinh(\gamma x) + c_{10}\cosh(\gamma x), \quad 0 \le x \le x_{bl} \tag{17}$$

$$M_{bl}(x) = -EIz''_{bl}(x), \quad 0 \le x \le x_{bl} \tag{18}$$

$$S_{bl}(x) = -EIz'''_{bl}(x), \quad 0 \le x \le x_{bl} \tag{19}$$

where x_{bl}, T_{bl}, c_7–c_9 are unknowns and $\gamma = \sqrt{\frac{T_{bl}}{EI}}$.

2.3.3. Touchdown section

The touchdown section models the part of the power cable resting on the seafloor i.e. from the TDP to the attachment point (AP) where the power cable is connected to a joint box, spanning x_a in length. The cable–soil interaction in this section is simplified by ignoring seabed friction and modelling the seabed with an elastic Winkler-type deformable soil model while the power cable in this section is considered in the framework of linear deformation beam theory. A zoomed in view of the touchdown zone—showing how the power cable is embedded in the soil, is depicted in Fig. 2. The governing equation of touchdown section is thus derived as the fourth-order ordinary differential equation given by Eq. (20).

$$EIz''''_{td}(x) - T_{bl}z''_{td}(x) + \mu z_{td}(x) = P, \quad x \le 0 \tag{20}$$

where μ is elastic stiffness of the soil (a value of 100 kPa is used in this study). Since frictional effect is neglected, the traction is constant along the beam. The general solution of Eq. (20) is given in Eq. (21) for which a real solution can only be obtained when the condition $T_{bl} \le 2\sqrt{EI\mu}$ is met—this condition was always satisfied in the computations done in this work.

$$\begin{aligned} z_{td}(x) = {} & \frac{P}{\mu} + c_{11}\, e^{\alpha x}\cos(\beta x) + c_{12}\, e^{\alpha x}\sin(\beta x) \\ & + c_{13}\, e^{-\alpha x}\cos(\beta x) + c_{14}\, e^{-\alpha x}\sin(\beta x), \quad x_a \le x \le 0 \end{aligned} \tag{21}$$

where c_{11}–c_{14} are the unknown coefficients, $\alpha = \frac{1}{2}\sqrt{2\sqrt{\frac{\mu}{EI}} + \frac{T_{bl}}{EI}}$ and $\beta = \frac{1}{2}\sqrt{2\sqrt{\frac{\mu}{EI}} - \frac{T_{bl}}{EI}}$.

Authors such as Lenci and Callegari (2005), Wang et al. (2019) adopted the approach of considering the elastic seabed on the negative side of the TDP to be infinite and as such the pipe laid on the seabed in their studies was treated as an infinite beam with the embedment depth, $d = P/\mu$ as $x \to -\infty$. With this, the coefficients c_{13} and c_{14} vanish from Eq. (21). For this study, we have a finite distance of x_a from the TDP to AP and as such the full Eq. (21) is employed. If the mechanical property of the part of the power cable close to the anchorage is not considered to be a design driver (this area is expected to experience negligible cyclic loading and bending unlike the section around the touchdown zone and the suspended parts), then such reduced form of Eq. (21) can be used. Initial studies not presented here however showed using the reduced form of Eq. (21) amounts to same results up to a short distance from AP.

The bending moment and shear for this section can be obtained with Eq. (22) and (23) respectively.

$$M_{td}(x) = -EIz''_{td}(x), \quad x_a \le x \le 0 \tag{22}$$

$$S_{td}(x) = -EIz'''_{td}(x), \quad x_a \le x \le 0 \tag{23}$$

2.4. Computation of horizontal and vertical separation

The vertical and horizontal separation i.e. Z_T the distance from HOP to the seabed and X_T the distance from HOP to AP are required inputs for the computation of the configuration and mechanical properties of the dynamic power cable. First, using the platform rigid body motions outputted from OpenFAST, we compute the position vector of the HOP relative to OpenFAST inertial reference frame. The OpenFAST inertial reference frame is represented here as (X^0, Y^0, Z^0)–the set of orthogonal axes of the inertial reference frame with the X^0Y^0-plane designating the Still Water Level (SWL) and the Z^0-axis pointing upwards along the centerline of the undisplaced Spar platform and in opposite direction to gravity (Jonkman, 2010). The computation of the position of the HOP in the X^0, Y^0, Z^0 frame is done using Eq. (24). Readers can refer to Spong et al. (2006) for details of coordinate transformation and formulation of rotation matrix which are not repeated here for sake of brevity.

$$p^0 = R_1^0 p^1 + d_1^0 \tag{24}$$

where p^0 is the column vector describing the position of the HOP relative to the inertial reference frame, p^1 is the position vector of the HOP relative to the platform reference frame (for this study, $p^1 = [0, 0, -120]^T$), R_1^0 is the platform rotation matrix given in Eq. (25) and

d_1^0 is the row vector whose elements are the platform translational surge, sway and heave motions.

$$\mathbf{R_1^0} = \begin{pmatrix} \cos\psi\cos\theta & \cos\psi\sin\theta\sin\phi - \sin\psi\cos\phi & \cos\psi\sin\theta\cos\phi + \sin\psi\sin\phi \\ \sin\psi\cos\theta & \sin\phi\sin\theta\sin\phi + \cos\psi\cos\phi & \sin\psi\sin\theta\cos\phi - \cos\psi\sin\phi \\ -\sin\theta & \cos\theta\sin\phi & \cos\theta\cos\phi \end{pmatrix} \tag{25}$$

where ϕ, θ, ψ are the platform roll, pitch, and yaw Euler angles. With p^0 calculated, we can obtain the vertical separation Z_T and the horizontal separation X_T with Eq. (26) and (27) respectively.

$$Z_T = (p^0 - x_{AP}^0) \cdot z \tag{26}$$

$$X_T = \sqrt{|p^0 - x_{AP}^0|^2 - Z_T^2} \tag{27}$$

where x_{AP}^0 is the position vector of the fixed point AP relative to the inertial reference frame (in this study $x_{AP}^0 = [400, 0, -320]$) and $z = [0, 0, 1]^T$ (unit vector pointing vertically upwards).

2.5. Boundary conditions (BCs)

The governing equations described in Section 2.3 amount to 22 unknowns: c_1–c_{14}, δ_1–δ_3, x_1–x_3, x_{bl}, T_{bl} which can be determined by boundary conditions. At the HOP, the elevation from the seabed is known as Z_T. Assuming that the hang-off angle, Φ_h is known, we obtain the BCs in Eq. (28) according to the global coordinate system (X, Z).

$$HOP \begin{cases} z_{hos}(x_1 + x_2 + x_3 + x_{bl}) = Z_T \\ z'_{hos}(x_1 + x_2 + x_3 + x_{bl}) = \tan(\Phi_h) \\ M_{hos}(x_1 + x_2 + x_3 + x_{bl}) = 0 \end{cases} \tag{28}$$

At the LP and DP, the continuity of displacement, inclination angle, curvature and tension is guaranteed according to the global coordinate system (X, Z) given by the equations below:

$$LP \begin{cases} z_{hos}(x_2 + x_1 + x_{bl}) = z_{bs}(x_2 + x_1 + x_{bl}) \\ z'_{hos}(x_2 + x_1 + x_{bl}) = z'_{bs}(x_2 + x_1 + x_{bl}) \\ T_{hos}(x_2 + x_1 + x_{bl}) = T_{bs}(x_2 + x_1 + x_{bl}) \end{cases} \tag{29}$$

$$DP \begin{cases} z_{bs}(x_1 + x_{bl}) = z_{ds}(x_1 + x_{bl}) \\ z'_{bs}(x_1 + x_{bl}) = z'_{ds}(x_1 + x_{bl}) \\ T_{bs}(x_1 + x_{bl}) = T_{ds}(x_1 + x_{bl}) \end{cases} \tag{30}$$

For the BLE, the continuity of displacement, inclination angle, curvature, shear and tension is guaranteed according to the global coordinate system (X, Z) given by the equations below:

$$BLE \begin{cases} z_{ds}(x_{bl}) = -z_{bl}(x_{bl}) \\ z'_{ds}(x_{bl}) = -z'_{bl}(x_{bl}) \\ M_{ds}(x_{bl}) = M_{bl}(x_{bl}) \\ S_{ds}(x_{bl}) = S_{bl}(x_{bl}) \\ T_{ds}(x_{bl}) = T_{bl} \end{cases} \tag{31}$$

At the TDP also, the continuity of displacement, inclination angle, curvature and shear is guaranteed according to the global coordinate system (X, Z) given by the equations below:

$$TDP \begin{cases} z_{bl}(0) = z_{td}(0) = 0 \\ z'_{bl}(0) = z'_{td}(0) \\ M_{bl}(0) = M_{td}(0) \\ S_{bl}(0) = S_{td}(0) \end{cases} \tag{32}$$

Finally at AP, from the displacement we obtain:

$$AP \left\{ -z_{td}(x_1 + x_2 + x_3 + x_{bl} - X_T) = 0, \right. \tag{33}$$

Recall Fig. 1, where it can be seen that $[x_1 + x_2 + x_3 + x_{bl} - X_T] = x_a$.

Two additional equations are needed to solve the highly nonlinear system of equations. These are derived by considering that the total arc length of the hang-off catenary S_{hos} and that of the buoyancy catenary S_{bs} are known and are assumed to be inextensible. Since $ds^2 = dx^2 + dz^2$, we can then obtain:

$$\frac{ds}{dx} = \sqrt{1 + [z'(x)]^2}$$

For the hang-off catenary section, $[z'_{hos}(x)]^2 = \sinh^2(\delta_1 x + c_2)$, applying the trigonometrical relationship $\sinh^2(\delta_1 x + c_2) = \cosh^2(\delta_1 x + c_2) - 1$, we derive:

$$\frac{ds}{dx} = \sqrt{\cosh^2(\delta_1 x + c_2)} = \cosh(\delta_1 x + c_2)$$

The arc length of the hang-off catenary can then be formulated as the definite integral from $(x_2 + x_1 + x_{bl})$ to $(x_3 + x_2 + x_1 + x_{bl})$ as shown in Eq. (34) below:

$$\begin{aligned} S_{hos} &= \int_{(x_2+x_1+x_{bl})}^{(x_3+x_2+x_1+x_{bl})} \cosh(\delta_1 x + c_2)\, dx \\ &= \frac{1}{\delta_1}\left(\sinh(c_2 + [x_3 + x_2 + x_1 + x_{bl}]\delta_1) - \sinh(c_2 + [x_2 + x_1 + x_{bl}]\delta_1)\right) \end{aligned} \tag{34}$$

Similarly we can obtain the total arc length of the buoyancy catenary as:

$$\begin{aligned} S_{bs} &= \int_{(x_1+x_{bl})}^{(x_2+x_1+x_{bl})} \cosh(\delta_2 x + c_4)\, dx \\ &= \frac{1}{\delta_2}\left(\sinh(c_4 + [x_2 + x_1 + x_{bl}]\delta_2) - \sinh(c_4 + [x_1 + x_{bl}]\delta_2)\right) \end{aligned} \tag{35}$$

With Eq. (28)–(35) we can solve for the 22 unknowns if the hang-off inclination Φ_h is known a priori. However, Φ_h in Eq. (28) is unknown. The solution method for obtaining all the unknowns is presented in the next section.

2.6. Solution algorithm

The system of equations presented in Section 2.5 is highly nonlinear and no explicit solution can be found. The methodology developed for solving this nonlinear system of equations is discussed subsequently with a flowchart of the solution scheme presented in Fig. 3. Let us assume for now that Φ_h is known. By applying algebraic manipulations, the system of 22 equations can be simplified to a system of 3 equations. Firstly, with the BCs at AP and TDP, the coefficients $c_7, c_8, c_9, c_{11}, c_{12}$, and c_{13} are expressed in terms of c_{10}, T_{bl} and x_a, with $c_{14} = 0$ (Note $x_a = (x_1 + x_2 + x_3 + x_{bl}) - X_T$ and using algebraic manipulations of equations within Eq. (30)–(35), x_1, x_2, x_3 are expressed in terms of δ_3 and Φ_h). From $T_{ds}(x_{bl}) = T_{bl}$ at the BLE, we obtain $\cosh(c_6 + x_{bl}\delta_3) = (T_{bl}\delta_3)/P$. Substituting this into $M_{ds}(x_{bl}) = M_{bl}(x_{bl})$, we derive $-z''_{bl} = P^2/(\delta_3 T^2)$ from which $c_{10} = c_{10}(T_{bl}, x_{bl}, \delta_3)$. In similitude with the derivation of the core problem done in Lenci and Callegari (2005), we derive Eq. (36) and (37) from the BLE BCs as:

$$f_1(T_{bl}, x_{bl}, \delta_3) = z''_{bl}(x_{bl})\sqrt{1 + [z'_{bl}(x_{bl})]^2} + \frac{P}{T_{bl}} = 0 \tag{36}$$

$$f_2(T_{bl}, x_{bl}, \delta_3) = z'''_{bl}(x_{bl}) + 2\, z'_{bl}(x_{bl})[z''_{bl}(x_{bl})]^2 = 0 \tag{37}$$

To derive the third equation required, we equate 2 expressions for c_5:

1. At BLE, $c_5(T_{bl}, x_{bl}, \delta_3) = -(T_{bl}/P) - z_{bl}(x_{bl})$, obtained by substituting $\cosh(c_6 + x_{bl}\delta_3) = (T_{bl}\delta_3)/P$ into $z_{ds}(x_{bl}) = -z_{bl}(x_{bl})$ and solving for c_5.
2. Using Eq. (30)–(35) we obtain $c_5(\delta_3, \Phi_h)$. Again, by assuming Φ_h is known, then $c_5 = c_5(\delta_3)$

The third equation is given thus:

$$f_3(T_{bl}, x_{bl}, \delta_3) = -[(T_{bl}/P) + z_{bl}(x_{bl}) + c_5(\delta_3)] \tag{38}$$

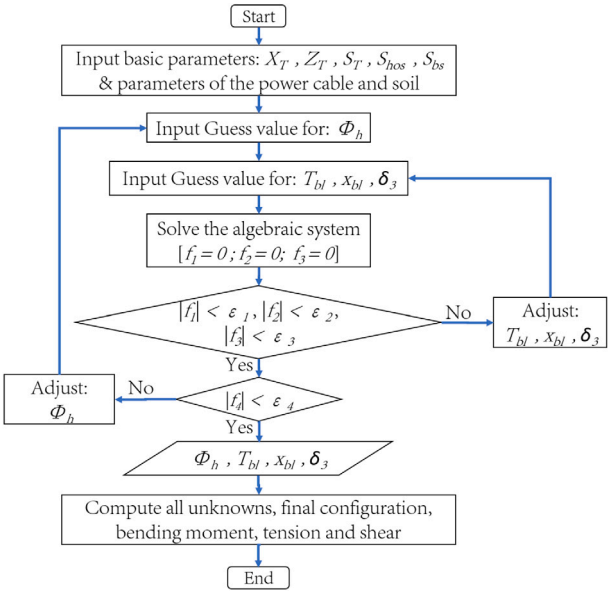

Fig. 3. Flow scheme of the solution procedure.

In this study, Newton–Raphson method is employed in solving Eq. (36)–(38). The error threshold $\epsilon_1 = \epsilon_2 = \epsilon_3 = 1 \times 10^{-7}$ is compared to evaluations of f_1, f_2, f_3 respectively to check the solution accuracy.

In reality, Φ_h is not known. To obtain the value of Φ_h, a value within the range 80°–89° is first assumed, it is then adjusted until the computed total arc length of the power cable ($S^*_{hos}+S^*_{bs}+S^*_{ds}+S^*_{bl}+S^*_{td}$) matches the known total arc length S_T with an error less than ϵ_4 ($\epsilon_4 = 1 \times 10^{-6}$). The function evaluated is represented by Eq. (39):

$$f_4(T_{bl}, x_{bl}, \delta_3) = S_T - (S^*_{hos} + S^*_{bs} + S^*_{ds} + S^*_{bl} + S^*_{td}) \tag{39}$$

where S^*_{hos}, S^*_{bs}, and S^*_{ds} are computed arc lengths for respective sections given T_{bl}, x_{bl}, δ_3 with similar formulation as Eq. (34) (since obtaining the required integrals is straightforward). For the arc lengths of the boundary-layer and touch down sections, the integration presented by $\int \sqrt{1 + [z'_{bl}(x)]^2}dx$ and $\int \sqrt{1 + [z'_{td}(x)]^2}dx$ respectively is difficult to solve, with Taylor series approximation not converging in most cases. Using discrete points, an arc length finding algorithm deployed as a MATLAB function call is employed in computing S^*_{bl} and S^*_{td}. The whole process takes around 3 min on an Intel (R) Core (TM) computer with specification: i5-8250U, 1.60 GHz, and 8G RAM. When compared with an OrcaFlex FEM model, the scheme presented here estimates Φ_h values to less than 0.1% difference from those computed by OrcaFlex (further comparisons are presented in Section 3).

A bilinear interpolation in similitude with those used by OrcaFlex Software (Orcina LTD, 2016) for solution of analytical line is employed. First a solution grid in space is established. The analytical model is then used to obtain $f^i_n(X, Z)$ for each point on the grid such that $f^i_n(X, Z)$ is a function that takes the horizontal and vertical cable separation as arguments and outputs i cable particular at a given arc length n. Using these functions, we then employ bilinear interpolation to compute the cable loads at selected arc lengths.

This enables easy and quick transformation of time series of platform motions outputted by OpenFAST into any chosen cable loading at selected arc lengths.

3. Model verification

The developed analytical model is applied to the NREL's 5MW wind turbine (Jonkman et al., 2009) mounted on the OC3-Hywind spar-type platform (Jonkman, 2010). For brevity sake, the parameters of the turbine are not repeated here, readers can refer to Jonkman et al. (2009), Jonkman (2010) for details. The spar buoy is a ballast stabilized slender draft hull with catenary mooring system for station keeping. The OC3-Hywind spar-supported FWT is suitable for water depths in the 200 m to 700 m range. For this study, analysis are performed with a water depth of 320 m. The properties of the power export cable which is attached to the platform are given in Table 1. The FWT and power cable are depicted in the OrcaFlex model shown in Fig. 4. The total length of the power cable in this study (S_T) is 550 m. The length of the hang-off section (S_{hos}) is 150 m while the length of the buoyancy section (S_{bs}) is 100 m. As mentioned in Section 2.4, the power cable HOP is located at (0 m, 0 m, −120 m)–the base of the spar platform, and the cable anchorage at the seabed is located at (400 m, 0 m, −320 m).

Table 1
Dynamic power cable properties.
Source: 2-armoured cable properties adapted from Ref. Martinelli et al. (2010).

Property	Unit	2-Armoured cable	Buoyancy section
Outside diameter	m	0.2	0.4
Submerged weight	N/m	390	−237
Bending Stiffness	kNm^2	10	10
Axial stiffness	MN	700	700
Minimum breaking load	kN	100	100
Minimum bending radius	m	2	2
Maximum allowable curvature	m^{-1}	0.5	0.5

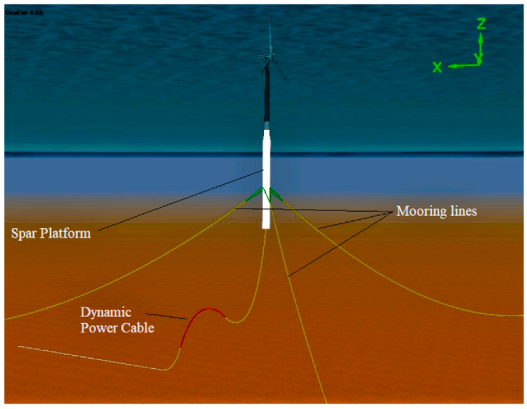

Fig. 4. OrcaFlex representation of the FWT model with dynamic power cable.

The assumption that the power cable does not significantly influence the dynamic response of the FWT system is the basis on which a decoupled analysis is employed. To investigate the strength of this assumption, two dynamic simulations with the same turbulent wind file and sea state as inputs are conducted in OrcaFlex. The mean wind speed at hub height is 10 m/s and the turbulence model is the IEC Extreme Turbulence Model (ETM). The wave height is 10 m and the peak period is 12 s. One model has the dynamic power cable attached to the platform while the other model does not have a power cable. A comparison between the platform motions for both cases is presented in Fig. 5.

The platform motions in Fig. 5 are transformed to horizontal and vertical separation of the cable and plotted in Fig. 6.

From Figs. 5 and 6, it is clear that the power cable has negligible influence on the dynamic response of the FWT system. The percentage error between the vertical and horizontal separation of the cable attachment point for the two cases (plotted in Fig. 6) are on average < 1%. Hence, a decoupled analysis is justified. Consequently, the same approach is continued for the surrogate-based reliability quantification proposed in this paper.

To verify the accuracy of the analytical model described in Sections 2.3–2.6, a comparison with an OrcaFlex FEM model is presented.

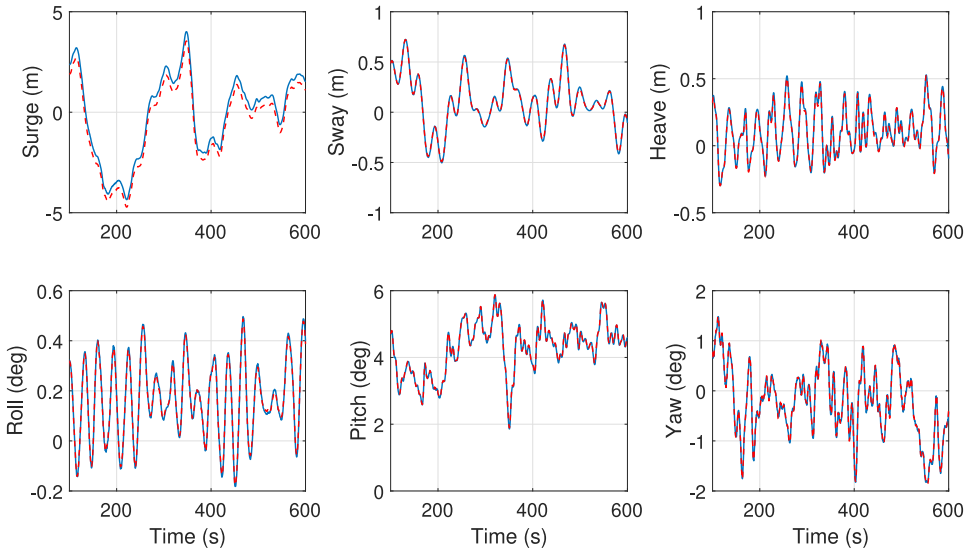

Fig. 5. Platform motions. The blue solid line is for the case where the FWT is modelled without a power cable and the red dashed line is the case where the power cable is modelled.

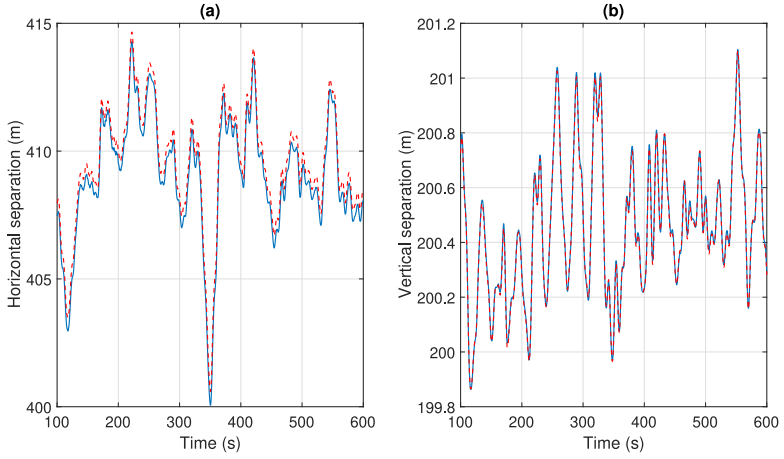

Fig. 6. Horizontal and vertical separation of the power cable attachment point. The blue solid line is for the case where the FWT is modelled without a power cable and the red dashed line is the case where the power cable is modelled.

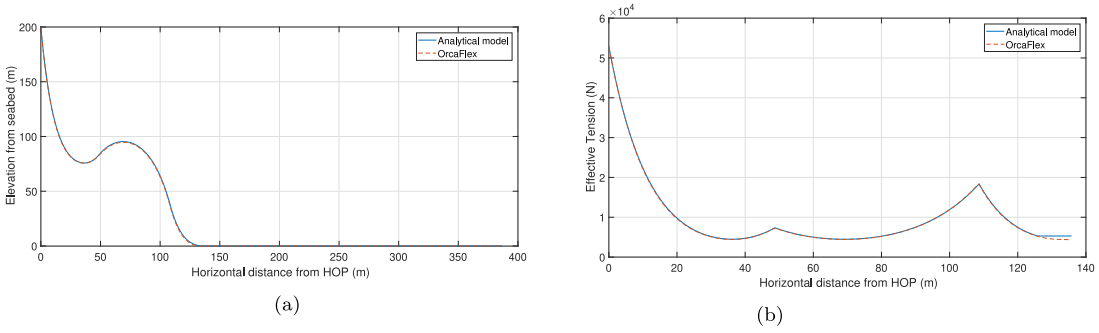

Fig. 7. (a) Lazy-wave configuration and (b) Effective Tension plotted against horizontal distance from HOP.

The lazy-wave configuration obtained with the proposed analytical model is compared to those obtained by OrcaFlex FE model in Fig. 7(a). This shows close match between both models. Fig. 7(b) shows the effective tension of the power cable, also showing good agreement between the two models.

The overestimation of the bending moment at TDP by Analytical model 2—where the entire length of the power cable is modelled with catenary equations is shown in Fig. 8. In Fig. 8 Analytical model 1 is the model described in this work and we can see that the model predicts the bending moment better than the use of full catenary implementation.

To further validate the use of the analytical model and subsequent bilinear interpolation, a comparison is presented in Fig. 9. The results in Fig. 9 are obtained with platform surge, sway and heave displacements as 22.22m, −0.3779m and −0.4931m respectively while the roll, pitch

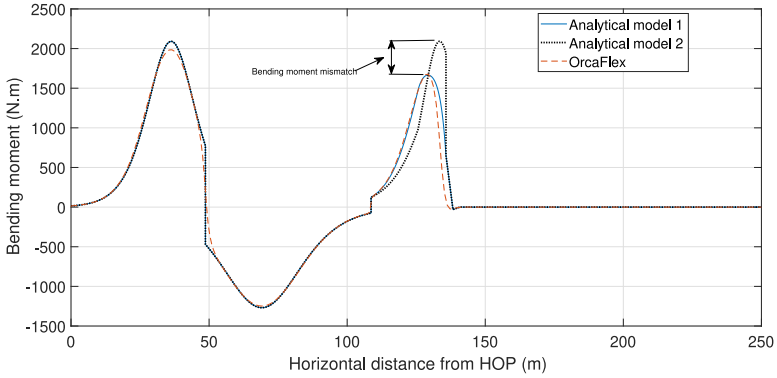

Fig. 8. Bending moment plotted against horizontal distance from HOP.

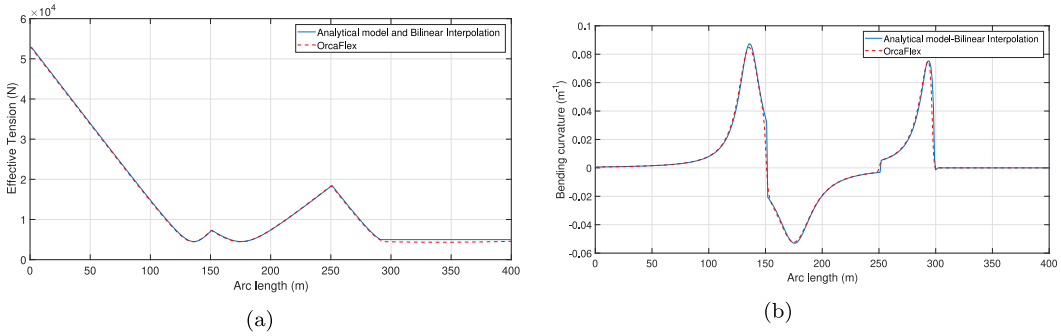

Fig. 9. (a) Effective Tension; (b) Bending curvature plotted against [0 m : 1 m : 400 m] arc length.

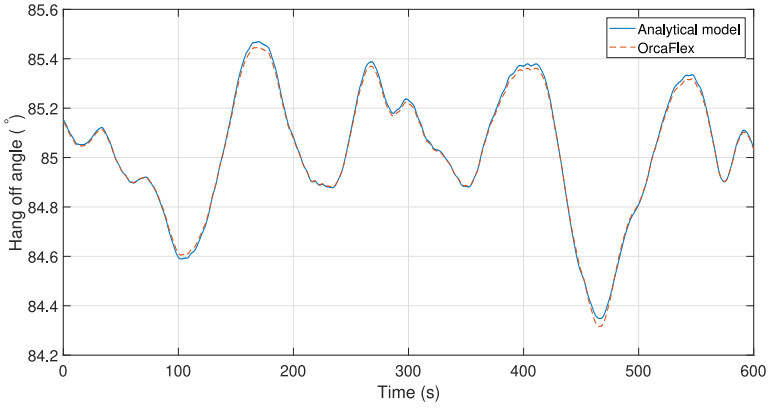

Fig. 10. Comparison of time series of hang-off angle.

and yaw rotations are 0.1793°, 4.289° and 0.01954° respectively. In Fig. 9, the effective tension and bending curvature are plotted for 400 m arc length measured from the HOP with 1 m increments.

The good match shown in Fig. 9 further validates the proposed approach and amounts to easy transformation of OpenFAST platform motion time series into time series of any chosen cable particulars. Using the time series of instantaneous motion of the spar platform outputted from OpenFAST, we compute the static state at each time step in OrcaFlex and with the analytical model as well. A comparison of the computed hang-off inclination from both models is given in Fig. 10. As shown in Fig. 10, the computed hang-off inclination for each time-step closely matches those computed by OrcaFlex, giving more validity to the proposed approach.

Overall, the methodology proposed in this paper leads to estimations of power cable loading that are on average 8% different from FE model by OrcaFlex but with significant computational savings.

4. Site specific environmental conditions

For accurate fatigue damage estimation, site specific environmental conditions have to be modelled and the resulting loads computed. Especially as floating wind turbines are exposed to a large variety of environmental conditions which contribute to the accumulation of damage at different rates throughout the lifetime of the turbine. In principle, one needs the site's long-term joint probability distribution model of relevant environmental parameters—capturing important multivariate dependencies as well. Simply put, it is essential to have an accurate model of the joint environmental conditions at the proposed site of deployment in order to obtain robust fatigue estimation that guarantees the safety and reliability of the turbine through out its service life.

The joint probabilistic model of wind and wave established by Johannessen et al. (2001) for sites in the northern North sea is adopted

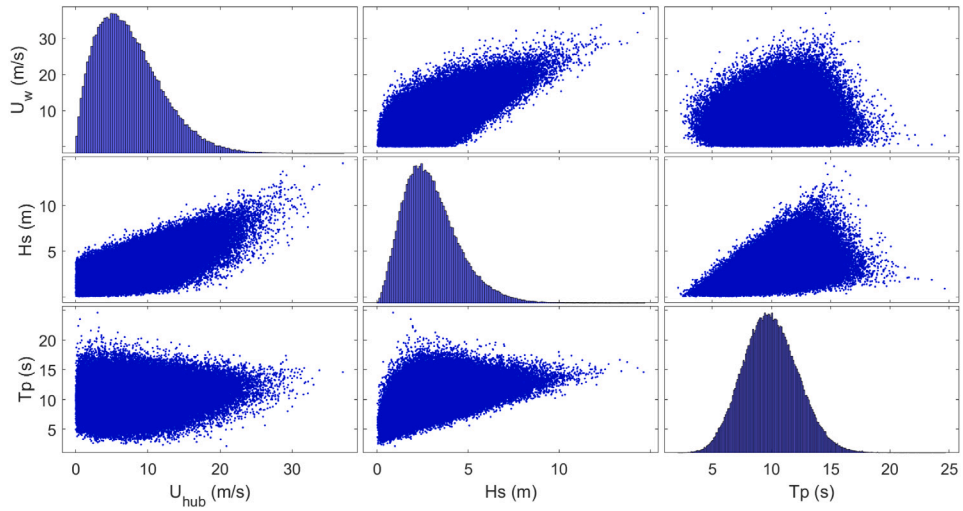

Fig. 11. Scatter plots and histograms of 20-year continuous MCS samples of U_w, H_s and T_p.

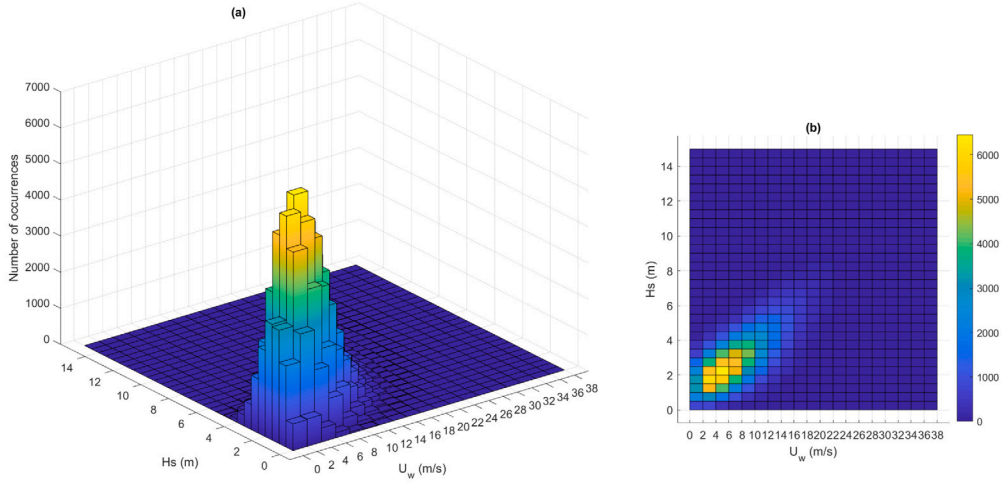

Fig. 12. Histogram showing occurrences of mean wind speed and wave height bins.

for the fatigue analysis presented in this paper. This joint distribution model is given by Eq. (40).

$$f_{U_w H_s T_p} = f_{U_w}(U_w) \cdot f_{H_s|U_w}(H_s|U_w) \cdot f_{T_p|U_w H_s}(T_p|U_w, H_s) \tag{40}$$

where $f(\cdot)$ is the probability distribution function.

The long-term distribution of wind and wave directions are not included in the probabilistic model of the environment. Hence, the influence of wind/wave directionality are ignored in the analysis conducted in this paper. Wind and wave are assumed to act in the same direction and are collinear. The marginal and conditional distributions that make up the joint probability distribution model in Eq. (40) are presented in Johannessen et al. (2001) and are not repeated here for sake of conciseness. Fig. 11 shows scatter plots and histograms of U_w, H_s and T_p samples generated from the joint environmental model. The dependencies between the environmental variables are visualized by the scatter plots in Fig. 11.

Also, the samples of the environmental variables are sorted into bins with bin sizes of 2 m/s for mean wind speed, 0.5 m for significant wave height and 0.5 s for peak spectral period. The joint occurrences of mean wind speed and significant wave height is shown in Fig. 12 while Fig. 13 shows the joint occurrence of significant wave height and peak spectral period.

For mean wind speed and significant wave height, the 4 m/s − 6 m/s mean wind speed bin with the 2 m − 2.5 m wave height bin have the highest frequency of occurrence of 6458. For significant wave height and peak spectral period, the 2 m−2.5 m wave height bin with the 8.5 s−9 s peak spectral period bin was the most frequent with occurrence of 2581.

5. Fatigue damage evaluation

5.1. Strain computation and ϵ-N curve

The main components of the power cable which are most susceptible to fatigue damage are the conductors, usually made of pure Electrolytic Tough Pitch (ETP) copper. Although copper has excellent conductivity, it has poor mechanical properties, which includes creeping or stress-relaxation and a stress–strain behaviour that is non-linear (Karlsen et al., 2009; Karlsen, 2010). Based on the creep and tensile properties of ETP copper which necessitates the consideration of the effect of plastic straining in the fatigue analysis of the conductor, Karlsen (2010) posited that an ϵ-N (strain versus number of cycles to failure) fatigue curve is better suited for fatigue analysis of the copper conductor than the traditional S-N (stress versus number of cycles to failure) curve. An ϵ-N curve accounts for both elastic strain (ϵ_e) and plastic strain (ϵ_p). It

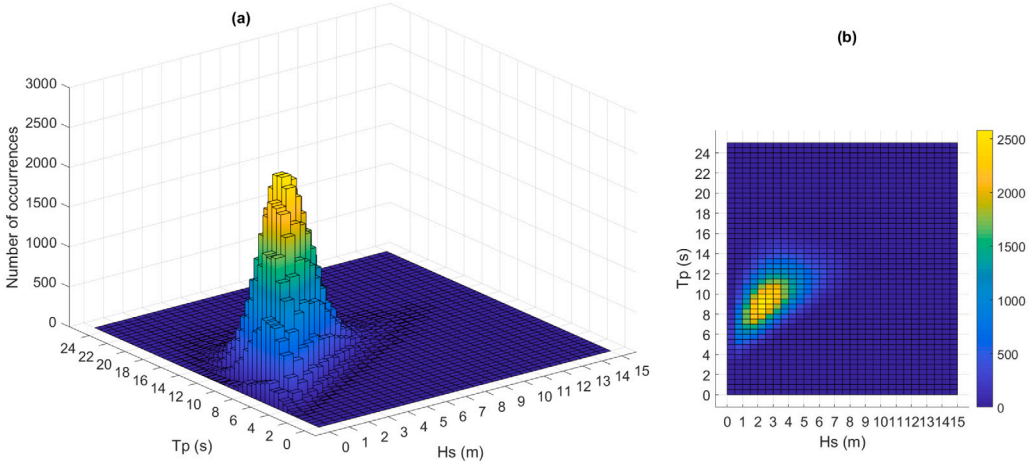

Fig. 13. Histogram showing occurrences of wave height and peak period bins.

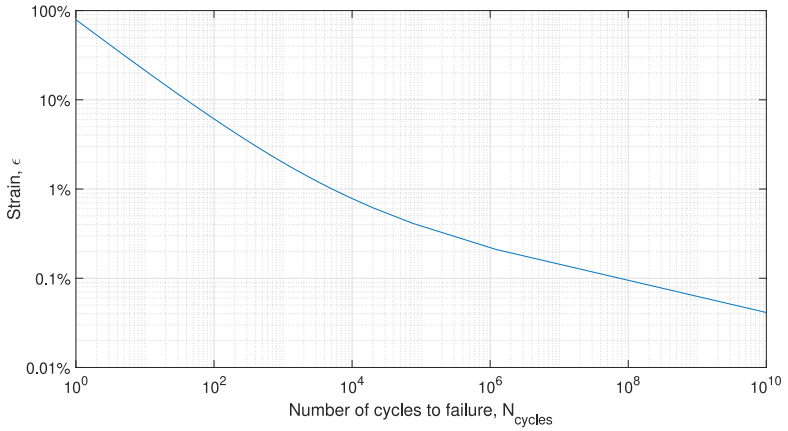

Fig. 14. Strain vs. Number of cycles for ETP copper conductor.
Source: Adapted from Karlsen et al. (2009).

can be expressed according to the Coffin–Manson relationship (Dieter and Bacon, 1986) given by Eq. (41).

$$\epsilon(N_{cycles}) = \epsilon_e(N_{cycles}) + \epsilon_p(N_{cycles}) = C_1 N_{cycles}^{-\beta_1} + C_2 N_{cycles}^{-\beta_2} \tag{41}$$

where $\epsilon(N_{cycles})$ is the strain amplitude resulting in failure at N_{cycles}, and C_1, C_2, β_1 and β_2 are material constants. The values of C_1, C_2, β_1 and β_2 for a typical power export cable for FWT application are given in Thies et al. (2012) as $C_1 = 0.7692, C_2 = 0.0219, \beta_1 = 0.5879$ and $\beta_2 = 0.1745$. The ϵ-N curve is reproduced here as shown in Fig. 14 and forms the basis for the fatigue analysis performed in this paper.

Using the computational model described in Section 2, the time series of platform motions from OpenFAST simulations of DLC1.2 of IEC 61400-3 (IEC, 2005) are transformed to time series of curvature and axial tension for points 0 m : 1 m : 400 m arc lengths of the power cable, from which strain time series, $\epsilon(t)$ are computed according to Eq. (42).

$$\epsilon(t) = \left[\kappa(t)\left(\frac{D_e}{2}\right) + \frac{N(t)}{EA}\right] \tag{42}$$

where κ is the bending curvature, EA is axial stiffness ($EA = 700MN$), D_e is the cable's effective diameter and N is axial tension. It takes around 2 s to transform a 3600 s long platform motion time series from OpenFAST to time series of effective tension, curvature and strain for the 400 discrete points along the cable. Fig. 15 shows such time series for 137 m arc length (this point is in the sag bend area).

For Fig. 15, D_e was set to the cable's outer diameter, OD. The environmental conditions are hub wind speed of 9.9 m/s, significant wave height of 2.2 m and peak period of 8 s.

In the reliability analysis conducted in this paper, the effective diameter of the cable (D_e) is treated as a random parameter. This is to account for uncertainty in determining the friction factor between wires. It was posited by Karlsen (2010) that the cable deformation (ϵ) would be between that of an imaginary ideal case of zero friction and that of an imaginary case of extreme friction as given by Eq. (43):

$$\kappa\frac{D_e}{2} < \epsilon < \kappa\frac{OD}{2} \tag{43}$$

where κ is the bending curvature. A fraction of the cable's outer diameter has to be chosen as D_e so as to fall within the boundaries of Eq. (43). An analysis is conducted in Section 6.2 to investigate the sensitivity of lifetime cable damage to the fraction of the cable's outer diameter used for calculating D_e.

5.2. Short-term fatigue damage of power export cable

Applying the computational frameworks developed in Section 2, the time series of platform motions from OpenFAST simulations are transformed to time series of curvature and axial tension for points 0 m : 1 m : 400 m arc lengths of the power cable, from which strain time series are computed. Given that the strain time series are irregular, Rainflow counting is employed to break down the fluctuations in the strain time series to individual hysteresis cycles. Considering the work

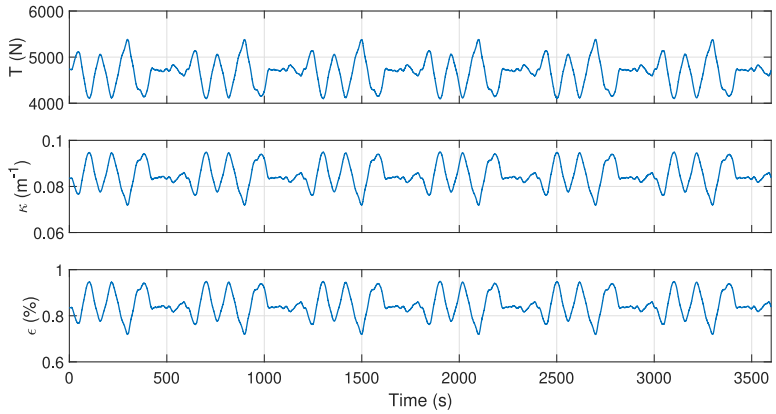

Fig. 15. Time series of effective tension, bending curvature and elastic strain for arc length 137 m from the HOP.

of Bathias (Bathias, 1999), the strain level below which the amplitudes from Rainflow counting are neglected is lowered to a small value of 0.01%. In other words, infinite fatigue life is assumed for strain amplitudes less than this threshold. Also, Goodman correction is applied to the strain amplitudes using an ultimate strain value of 1%.

After Rainflow counting, short-term fatigue damage (fatigue damage valid for the simulation time) is then computed by applying Miner's cumulative damage model according to Eq. (44).

$$D_j = \sum_i \frac{1}{N_{cycles_i}(\epsilon_i)} \tag{44}$$

where ϵ_i is the ith strain amplitude, and N_{cycles_i} is the number of cycles to failure for ϵ_i.

For a chosen number of cycles N_{eq}, the short-term damage given by Eq. (44) can be converted to damage equivalent stress with the following computations. First we consider the expressions below:

$$N_{eq} \cdot \frac{1}{N_{cycles_{EQ}}} = \sum_i \frac{1}{N_{cycles_i}(\epsilon_i)} \tag{45}$$

Eq. (45) can then be expressed in terms of $N_{cycles_{EQ}}$ as:

$$N_{cycles_{EQ}} = \frac{N_{eq}}{\sum_i \frac{1}{N_{cycles_i}(\epsilon_i)}} = \frac{N_{eq}}{D_j} \tag{46}$$

where $N_{cycles_{EQ}}$ is the number of cycles corresponding to the strain range ϵ_{EQ} which causes the same amount of damage as the real strain spectrum with several strain levels.

Since, N_{eq} can be chosen arbitrarily (in this study $N_{eq} = 3600$), and D_j can be computed, a value for $N_{cycles_{EQ}}$ can thus be obtained. Using the value of $N_{cycles_{EQ}}$, the damage equivalent strain, ϵ_{EQ} is estimated by numerically solving the nonlinear relationship given by Eq. Eq. (41). This damage equivalent strain is converted to damage equivalent stress σ_{EQ} by multiplying with Young's Modulus, $E = 128$ GPa.

5.3. Long-term fatigue damage

The long-term fatigue damage can be computed by taking the integral of the short-term damage over the joint distribution of input random variables X as given below:

$$D_{Life} = \frac{T_{Life}}{T_{sim} \cdot N_{seeds}} P_{lc} \alpha_{pwr} \int_{-\infty}^{\infty} D(X) f(X_{env}) dx \tag{47}$$

where X comprises environmental input variables X_{env} described in Section 4 and material and geometric random variables. Table 2 summarizes the input random variables used in this study. The parameter $\frac{T_{Life}}{T_{sim} \cdot N_{seeds}}$ is a scaling factor, converting from simulation time ($T_{sim} \times N_{seeds}$) to a design lifetime (T_{Life}). The parameter T_{sim} is the length of the time series used for Rainflow counting, while N_{seeds} is the number of wind/wave seeds used, which is six. The lifetime, $T_{Life} = 365 \times 24 \times 3600$ s, corresponds to annual lifetime in seconds. The frequency of occurrence of the environmental states is $f(X_{env})$, P_{lc} is the probability of occurrence of the considered load case (power production load case), and α_{pwr} is the availability factor. Adding P_{lc} to the formulation accounts for the amount of time the environmental conditions fall within those prescribed for the power production load case. The availability term, α_{pwr} accounts for the proportion of time within this environmental window that a turbine is technically capable of producing power. Typically current offshore wind farms achieve availability around 90% (Hassan, 2013). This value is assumed to be the availability of the studied wind turbine.

The integral in Eq. (47) can be approximated with Monte Carlo simulations as the arithmetic mean given below:

$$D_{Life} = \frac{T_{Life}}{T_{sim} \cdot N_{seeds}} \frac{1}{N} P_{lc} \alpha \sum_j^N D(X_j) \tag{48}$$

In this work, 2,000,000 samples are used (i.e $N = 2,000,000$) for evaluating Eq. (48). The samples are drawn using Monte Carlo Sampling (MCS) of the distributions of environmental, material and geometric uncertainties given in Table 2. For each sample point, the trained and validated Kriging metamodel (discussed in Section 6.2) is used to predict the corresponding short term damage equivalent stress, σ_{krig}. To account for uncertainties which encumber the accuracy of the computation of σ_{krig}, unique realizations from the distributions of relevant uncertainties (discussed subsequently and given in Table 2) are used as multipliers on σ_{krig} to give σ_{EQ} as described in Eq. (49). Once these uncertainties have been applied, using σ_{EQ}, the procedure described in Section 5.2 is reversed to obtain the short term fatigue damage for each sample point. From the short term fatigue damage, long term damage is obtained with Eq. (48).

$$\sigma_{EQ} = \sigma_{krig} \cdot (X_{dyn} X_{str} X_{exp} X_{aero} X_{hydo}) \tag{49}$$

where X_{dyn} is the uncertainty related to dynamic response modelling of the wind turbine which covers uncertainty in eigenfrequencies and damping ratios, X_{str} models uncertainty related to the computation of load-effects, X_{exp} accounts for uncertainty associated with site assessment such as topography and terrain roughness. The use of quasi-steady Blade Element Momentum (BEM) theory and assessment of aerodynamic drag and lift coefficients introduces uncertainty which is modelled by X_{aero} while uncertainty related to the assessment of hydrodynamic drag and inertia coefficients is modelled by X_{hydro}. The uncertainties in Eq. (49) are classed as epistemic uncertainties–uncertainties that arise from insufficient knowledge of the considered system or the environment (Sørensen and Toft, 2010).

The uncertainty related to the use of six wind and waves seeds in the dynamic aero-servo-elastic simulations used for training the Kriging metamodel is captured by X_{seeds} and is applied to the lifetime damage in Section 7. This was established from outputs of a previous

Table 2
Random variables used for surrogate model training and fatigue reliability analysis.

Variable	Dist	Ref	Dep	Parameters
Mean wind speed, U_w	W	Johannessen et al. (2001)	–	$\alpha = 1.708$, $\beta = 8.426$
Significant wave height, H_s	W	Johannessen et al. (2001)	U_w	–
Peak spectral period, T_p	LN	Johannessen et al. (2001)	U_w, H_s	–
Tower Young's modulus, E_t	N	Yang et al. (2015), Jonkman (2010)	–	$\mu = 210$ GPa, $CoV = 0.05$
Tower base thickness, t_t	N	Yang et al. (2015), Jonkman (2010)	–	$\mu = 0.027$ m, $CoV = 0.03$
Tower density, ρ_t	N	Yang et al. (2015), Jonkman (2010)	–	$\mu = 8500$ kg/m^3, $CoV = 0.05$
Mooring diameter, D_m	N	Jonkman (2010)	–	$\mu = 0.09$ m, $CoV = 0.03$
Power cable effective diameter, D_e	N	N/A	–	$\mu = f_{OD} \times 0.2$ m, $CoV = 0.03$
Exposure (terrain), X_{exp}	LN	Abdallah et al. (2015)	–	$\mu = 1$, $CoV = 0.1$
Structural dynamics, X_{dyn}	LN	Tarp-Johansen (2005), Abdallah et al. (2015)	–	$\mu = 1$, $CoV = 0.05$
Aerodynamic parameters, X_{aero}	LN	Tarp-Johansen (2005), Abdallah et al. (2015)	–	$\mu = 1$, $CoV = 0.1$
Hydrodynamic parameters, X_{hydro}	LN	Tarp-Johansen (2005), Abdallah et al. (2015)	–	$\mu = 1$, $CoV = 0.1$
Use of six wind/wave seeds, X_{seeds}	N	N/A	–	$\mu = 1.057$, $CoV = 0.246$
Stress concentration factor, X_{SCF}	N	DNV (2015), Ambühl et al. (2015)	–	$\mu = 1$, $CoV = 0.1$
Fatigue resistance, X_δ	LN	Veritas and Lloyd (2010)	–	$\mu = 1.05$, $SD = 0.32$

Dist: Distribution; Ref: Reference; Dep: Dependency; N: Normal; LN: Lognormal;
W: Weibull;D: Deterministic; α : Shape parameter; β: Scale parameter;
μ: Mean; CoV: Coefficient of variation ; $f_{OD} = [45\% : 5\% : 95\%]$.

study (Okpokparoro and Sriramula, 2020). On the structural capacity side of the limit state formulation used for the estimation of failure probability presented in Section 7, the random variable, X_δ is used to model the uncertainty in fatigue damage resistance.

6. Kriging modelling

Kriging metamodel is used to predict the value of the short-term damage equivalent stress $\sigma_{krig}(\boldsymbol{x} = [U_w, H_s, T_p, E_t, t_t, \rho_t, D_m, D_e])$ which otherwise is computationally expensive to evaluate. Only a brief description is provided here. Copious details can be found in Santner et al. (2003), Lataniotis et al. (2015). The Kriging estimator is described by Eq. (50).

$$Y^*(\boldsymbol{x}) = \boldsymbol{\beta}^T \boldsymbol{f}(\boldsymbol{x}) + Z(\boldsymbol{x}) \tag{50}$$

where $Y^*(\boldsymbol{x})$ is the Kriging estimate, i.e. $\sigma_{EQ}(\boldsymbol{x})$ in this paper. The first term on the right hand side of Eq. (50) is the mean value or trend of the output consisting of N basis functions $f_i; i = 1, \ldots, N$ and corresponding regression coefficients $\beta_i; i = 1, \ldots, N$. Given in Eq. (51) and (52), are the trends for the ordinary Kriging and universal Kriging metamodels respectively. The simple Kriging is not covered for sake of brevity.

$$\boldsymbol{\beta}^T \boldsymbol{f}(\boldsymbol{x}) = \beta_0 \tag{51}$$

$$\boldsymbol{\beta}^T \boldsymbol{f}(\boldsymbol{x}) = \sum_{t=0}^{N} \beta_t f_t(x) \tag{52}$$

In the ordinary Kriging, the trend has a constant but unknown value. For universal Kriging, the trend is assumed to be a linear combination of arbitrary functions which can be linear, quadratic or any polynomial. The second term in Eq. (50) represents the Gaussian process described by a zero mean, variance σ^2 and covariance given by Eq. (53).

$$Cov(\boldsymbol{x}, \boldsymbol{x}') = \sigma^2 R(\boldsymbol{x}, \boldsymbol{x}', \boldsymbol{\theta}) \tag{53}$$

where R represents the correlation function having associated hyper-parameters $\boldsymbol{\theta}$. The correlation function R describes the correlation between $\boldsymbol{x}$ and $\boldsymbol{x}'$.

The Kriging module contained in the framework for uncertainty quantification toolbox developed by UQLab (Lataniotis et al., 2015), is used in this study. The toolbox provides options for optimization of Kriging hyper-parameters. Readers can refer to Lataniotis et al. (2015) for details.

6.1. Kriging model training and validation

The Kriging model employed in this study is trained using a training set of 2500 sample points. An additional set of 100 sample points and a separate set of 1000 samples are generated and used for calibrating the Kriging model and validating the generalization capability of the trained model. The samples are drawn using the variance reducing Latin Hypercube Sampling (LHS) method (Shields and Zhang, 2016). The training sample size of 2500 was chosen based on satisfying the condition that maximum Normalized Root Mean Squared Error (NRMSE) with the validation set is $< 1\%$. Each sample point is a realization of the vector of input random variables ($[U_w, H_s, T_p, E_t, t_t, \rho_t, D_m, D_e]$) and requires running six aero-hydro-servo-elastic simulations of 10-minutes duration in OpenFAST given six wind/wave seeds are used. These simulations are conducted following the set up for DLC1.2 in IEC 61400-3 (IEC, 2005). The analytical model developed in this paper is then used to estimate the strain time histories from which damage equivalent stress is computed.

In order to select a suitable Kriging model, the set of hyper-parameters that maximize the likelihood of observations is estimated using maximum likelihood method for different trends. The choice of appropriate trend, correlation function and sample size is a key challenge in calibration of the Kriging model. A combinatorial method similar to that employed by Morató et al. (2019), Slot et al. (2020), Okpokparoro and Sriramula (2021) is employed here in calibrating the

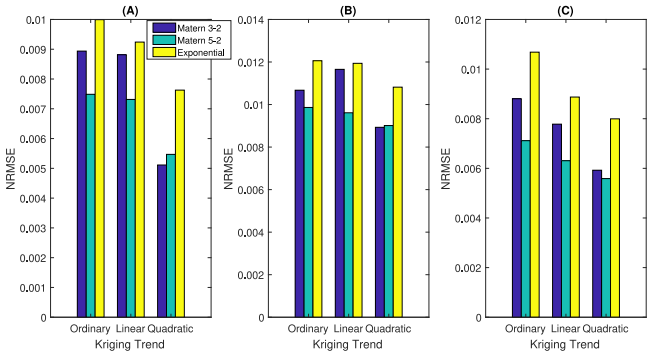

Fig. 16. Comparison of the performance of Kriging trends and correlation functions for equivalent stress range prediction at (a) Cable hog bend (arc length of 135 m, $S_{135\ \mathrm{m}}$); (b) Cable sag bend (arc length of 178 m, $S_{178\ \mathrm{m}}$); and (c) Cable touch down point (arc length of 292 m, $S_{292\ \mathrm{m}}$).

Kriging models. A comparison is made for combinations of Ordinary Kriging and universal Kriging (linear and quadratic trends) against Matérn-3/2, Matérn-5/2 and exponential in Fig. 16.

Overall, the Matérn-3/2 with a linear trend gave the best results for tower equivalent stress range predictions. For the mooring lines, the Matérn-5/2 with a quadratic trend amounted to the best Kriging model while on average the Matérn-3/2 with a quadratic trend amounted to the best predictive performance of the Kriging models. Using the calibrated Kriging models, predictions are made on an input data set comprising 1000 sample points for model testing.

One to one comparisons between the Kriging predictions and the validation data is presented in Fig. 17 . Also included in these plots are the computed NRMSE and the Coefficient of Determination (R^2). On average, from the R^2 values, the Kriging model explains more than 99.9% of the variability in the turbine responses considered. So also, very low NRMSE of $\approx<$ 1% are computed. This is a demonstration of the validity of the calibrated Kriging model.

6.2. Kriging for lifetime damage evaluation

The lifetime damage, D_{Life} of the cable is evaluated by integrating over the input domain (as described in Section 5.3 and given by Eq. (47)). The trained and adequately calibrated Kriging metamodel is used to approximate the short-term damage equivalent stress. This damage equivalent stress is then converted to short-term fatigue damage used in Eq. (47). The calculated values of D_{Life} at arc length 135 m, 178 m and 292 m (points in the hog bend, sag bend and touch down zone of the cable respectively) are presented in Fig. 18(a). Case 1 represents a situation where all relevant uncertainties in Table 2 are accounted for in the computation of D_{Life}. In Case 2, only the environmental variability is modelled. The effective cable diameter was taken as 50% of the cable's OD which amounted to a very conservative estimate of the fatigue damage. Fig. 18(b) shows the variation of annual fatigue damage with $\frac{D_e}{OD}$.

It is worth noting that accounting for relevant uncertainties as in Case 1 of Fig. 18(a) gave higher lifetime damage compared to a case where only environmental uncertainties are considered. The Case 1 values of D_{Life} are subsequently used for the evaluation of the probability of failure. Also, from Fig. 18(b), it is observed that using less than 60% of the cable's OD amounted to very conservative annual damage values. The severest damage as expected was for $\frac{D_e}{OD} = 0.95$. Thus, in the reliability analysis of the power cable conducted in the next section, the mean value of D_e is set as 95% of the cable's OD. The corresponding annual damage is 0.0218. This value is comparable to the outcomes of Sobhaniasl et al. (2020) within the assumptions of the respective studies. It was decided to use this worst case as the friction factor between the wires in this study is unknown.

7. Reliability analysis

The probability of failure during n years of operation can be represented as:

$$P_f = P\left[X_\delta \leq \left(X_{seeds} \cdot n \cdot D_{Life}\right)\right] \tag{54}$$

where X_{seeds} models the uncertainty related to the use of a given wind/wave seeds, X_δ is the fatigue resistance, and D_{Life} is the corresponding 1-year fatigue damage for the considered structural component. The failure probability can also be expressed as:

$$P_f = P\left[g \leq 0\right] \tag{55}$$

where g is the limit state function given by: $g = X_\delta - (X_{seeds} \cdot n \cdot D_{Life})$. The limit state function g can be evaluated by structural reliability methods such as First/Second Order Reliability Method, FORM/SORM, Monte Carlo Simulation (MCS), importance sampling etc. The reliability index, β can be obtained with Eq. (56).

$$\beta = -\Phi^{-1}(P_f) \tag{56}$$

where $\Phi^{-1}(\cdot)$ is the inverse of the standard normal cumulative distribution function. Readers can refer to Madsen et al. (2006) for copious details of structural reliability methods as these are not presented here for brevity sake. In this paper, FORM, SORM and MCS are employed. The annual and cumulative failure probability of the power cable at the hog bend is presented in Fig. 19.

The three structural reliability methods (FORM, SORM and MCS) show good agreement as can be seen in Fig. 19. The temporal evolution of cable's reliability index computed from the cumulative failure probabilities is shown in Fig. 20. The failure probability of the power cable remained below target levels up until year 13. This value increases to 14 years when material and geometric uncertainties are ignored.

The values of β_1 and β_2 in Fig. 20 differed by as much as 33%. These results show that the non-inclusion of material and geometric uncertainties in the estimation of reliability levels can amount to increased reliability levels which might not reflect reality. The results presented here do not account for dynamic effects and wave/current loading on the cable. This is due to the limitations of the quasi-static analytical model employed. Such effects can significantly increase fatigue damage and should be considered in final design stages using more robust models.

8. Conclusions

In this paper, an analytical model for the design of lazy-wave dynamic power cables is developed. The analytical model was shown to be capable of capturing important phenomena such as boundary-layer phenomenon and cable–soil interaction. Verification of the analytical model was done with comparison against FE model developed with the widely used offshore industry commercial tool, OrcaFlex. The proposed model showed good agreement—predicted values usually fall within 8% difference from OrcaFlex estimations. The efficient evaluation of the cable particulars from platform motion time series outputted by the aero-hydro-servo-elastic codes like OpenFAST or any other solver, implies huge computational savings and can be very useful in initial design phases for configuration optimization and model selection as well as for reliability analysis as demonstrated in this paper.

The reliability assessment presented here entailed the estimation of accumulated lifetime damage arising from uncertain environmental loading as well as randomness in material and geometric parameters. Kriging surrogate models were used to approximate short-term damage equivalent stress, enabling the integration of damage over the joint distribution of input random variables. The Kriging model showed good predictive ability, achieving R^2 values around 99.9% and very low NRMSE of $\approx<$ 1%. The reliability level of the power cable in terms of failure probability and reliability index was assessed afterwards.

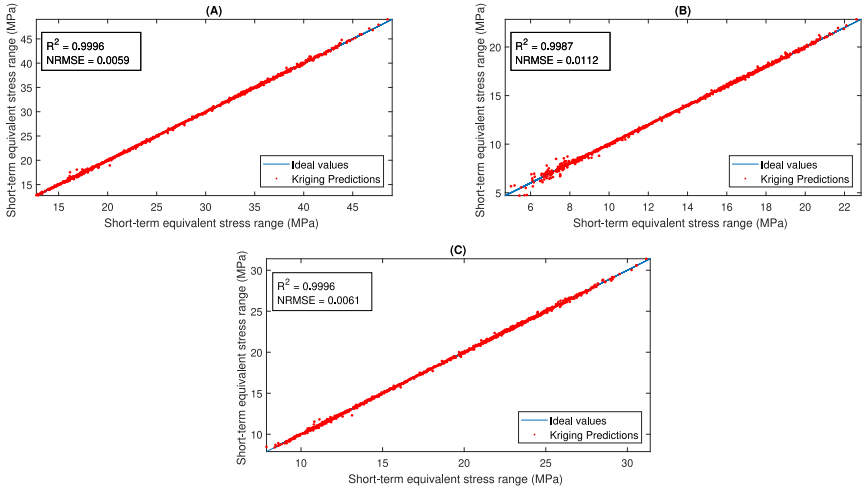

Fig. 17. Cross validation plots of cable short-term equivalent stress range for (a) Cable hog bend (arc length of 135 m, $S_{135\ \mathrm{m}}$); (b) Cable sag bend (arc length of 178 m, $S_{178\ \mathrm{m}}$); and (c) Cable touch down point (arc length of 292 m, $S_{292\ \mathrm{m}}$).

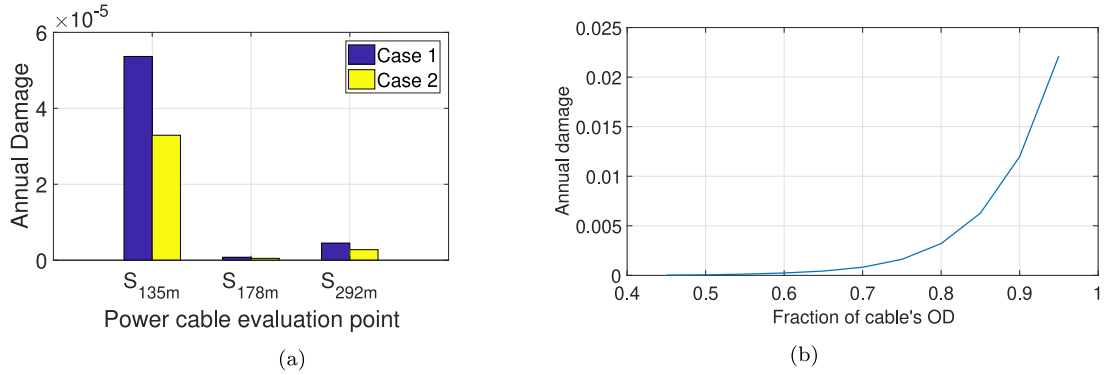

Fig. 18. (a) Annual damage ($D_e = 0.5OD$) (b) Annual fatigue damage as a function of $\frac{D_e}{OD}$.

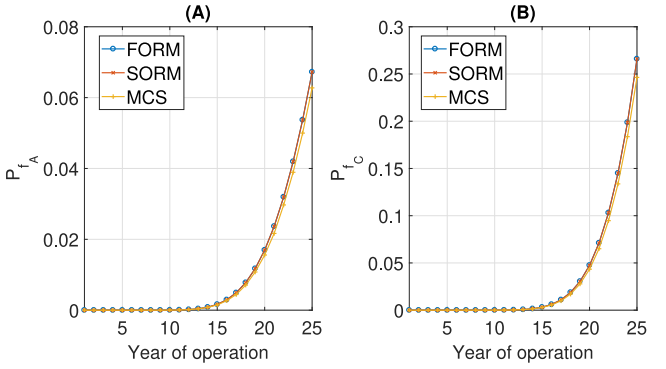

Fig. 19. (A) Cable annual failure probability; (B) Cable cumulative failure probability.

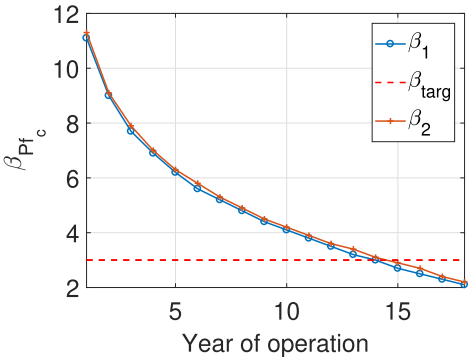

Fig. 20. Temporal evolution of cable's reliability index. Subscript 1 denotes a case where material and geometric uncertainties are modelled; 2 denotes the case where only environmental uncertainty is captured.

The cable was shown to fail at year 13 of operation when relevant uncertainties are considered. The cumulative failure probability after 25 years was greater than 25%. This is very high and is consistent with the frequent occurrence of power cable failures common in offshore wind farms. The methodology presented in this paper will no doubt enable the evaluation of the reliability levels attainable by dynamic power cables under site-specific metocean conditions. Extending the probabilistic reliability approach presented here with more robust cable models (capable of considering current and wave loads on the cable) will be helpful for final design phases and the calibration of partial safety factors for dynamic power cable design. To achieve a robust pathway for reliability quantification, the follow-up studies are now

focusing on improving the cable model, addressing the influence of ancillary structures (such as the lump mass and pontoons) on dynamic cable reliability as well as the cable response sensitivity to simulation length.

CRediT authorship contribution statement

Salem Okpokparoro: Methodology, Software, Validation, Investigation, Writing – original draft, Funding acquisition. **Srinivas Sriramula:** Conceptualization, Supervision, Writing – review & editing, Resources, Project administration.

Declaration of competing interest

The authors declare that they have no known competing financial interests or personal relationships that could have appeared to influence the work reported in this paper.

Data availability

Data will be made available on request.

Acknowledgements

The first author would like to thank the Petroleum Technology Development Fund (PTDF), Nigeria for the funding of this PhD research.

References

Abdallah, I., Natarajan, A., Sørensen, J.D., 2015. Impact of uncertainty in airfoil characteristics on wind turbine extreme loads. Renew. Energy 75, 283–300.
Ambühl, S., Ferri, F., Kofoed, J.P., Sørensen, J.D., 2015. Fatigue reliability and calibration of fatigue design factors of wave energy converters. Int. J. Mar. Energy 10, 17–38.
Bathias, C., 1999. There is no infinite fatigue life in metallic materials. Fatigue Fract. Eng. Mater. Struct. (Print) 22 (7), 559–565.
Bossanyi, E., 2015. GH Bladed user manual (version 4.7). Garrad Hassan Bladed.
Croll, J., 2000. Bending boundary layers in tensioned cables and rods. Appl. Ocean Res. 22 (4), 241–253.
Dieter, G.E., Bacon, D.J., 1986. Mechanical Metallurgy, Vol. 3. McGraw-hill New York.
DNV, G., 2015. Probabilistic Methods for Planning of Inspection for Fatigue Cracks in Offshore Structures. Standard No. DNVGL-RP-C210, DNV GL, Oslo, Norway.
DTU, 2021. HAWC2 - aeroelastic simulation of wind turbines. https://www.hawc2.dk/. (Accessed 07 December 2021).
GCube Insurance, 2019. Claims: offshore wind must quickly respond to changing global risk profile. http://www.gcube-insurance.com/offshore-wind-must-respond-risk/. (Accessed 20 January 2021).
Hassan, G.G., 2013. A Guide To UK Offshore Wind Operations and Maintenance. Scottish Enterprise.
IEC, 2005. IEC 61400-3: Wind Turbines–Part 1: Design Requirements, Vol. 64. International Electrotechnical Commission, Geneva.
IEC, 2019. IEC TS 61400-3-2: Wind Energy Generation Systems - Part 3-2: Design Requirements for Floating Offshore Wind Turbines. International Electrotechnical Commission.
Johannessen, K., Meling, T.S., Hayer, S., et al., 2001. Joint distribution for wind and waves in the northern north sea. In: The Eleventh International Offshore and Polar Engineering Conference. International Society of Offshore and Polar Engineers.
Jonkman, J., 2010. Definition of the Floating System for Phase IV of OC3. Technical Report, National Renewable Energy Lab.(NREL), Golden, CO (United States).
Jonkman, B.J., Buhl, Jr., M.L., 2006. TurbSim User's Guide. Technical Report, National Renewable Energy Lab.(NREL), Golden, CO (United States).
Jonkman, J., Butterfield, S., Musial, W., Scott, G., 2009. Definition of a 5-MW Reference Wind Turbine for Offshore System Development. Technical Report, National Renewable Energy Lab.(NREL), Golden, CO (United States).
Jonkman, B., Jonkman, J., 2016. FAST v8. 16.00 a-bjj. Natl. Renew. Energy Lab.
Karlsen, S., 2010. Fatigue of copper conductors for dynamic subsea power cables. In: International Conference on Offshore Mechanics and Arctic Engineering, Vol. 49149. pp. 275–281.
Karlsen, S., Slora, R., Heide, K., Lund, S., Eggertsen, F., Osborg, P.A., 2009. Dynamic deep water power cables. In: Proceedings of RAO/CIS Offshore 2009, Vol. 15. St Petersburg, Russia, pp. 194–203.
Lataniotis, C., Marelli, S., Sudret, B., 2015. UQLab User Manual–The Input Module. Report UQLab-V0, pp. 9–102.
Lenci, S., Callegari, M., 2005. Simple analytical models for the J-lay problem. Acta Mech. 178 (1), 23–39.
Li, X., Zhang, W., 2020. Long-term fatigue damage assessment for a floating offshore wind turbine under realistic environmental conditions. Renew. Energy 159, 570–584.
Madsen, H.O., Krenk, S., Lind, N.C., 2006. Methods of Structural Safety. Courier Corporation.
Martinelli, L., Lamberti, A., Ruol, P., Ricci, P., Kirrane, P., Fenton, C., Johanning, L., 2010. Power umbilical for ocean renewable energy systems-feasibility and dynamic response analysis. In: Proc. Int Conf Ocean Energy.
Morató, A., Sriramula, S., Krishnan, N., 2019. Kriging models for aero-elastic simulations and reliability analysis of offshore wind turbine support structures. Ships Offshore Struct. 14 (6), 545–558.
Murcia, J.P., Réthoré, P.-E., Dimitrov, N., Natarajan, A., Sørensen, J.D., Graf, P., Kim, T., 2018. Uncertainty propagation through an aeroelastic wind turbine model using polynomial surrogates. Renew. Energy 119, 910–922.
Okpokparoro, S., Sriramula, S., 2020. Ultimate loads and fatigue damage convergence of floating wind turbine components. In: Proceedings of the 30th European Safety and Reliability Conference and the 15th Probabilistic Safety Assessment and Management Conference. pp. 1004–1010.
Okpokparoro, S., Sriramula, S., 2021. Uncertainty modeling in reliability analysis of floating wind turbine support structures. Renew. Energy 165, 88–108.
Orcina LTD, 2016. OrcaFlex User Manual Version 11.0 b. Orcina Ulverston, UK.
Quéau, L.M., Kimiaei, M., Randolph, M.F., 2013. Lazy wave catenary risers: Scaling factors and analytical approximation of the static stress range in the touchdown zone. In: International Conference on Offshore Mechanics and Arctic Engineering, Vol. 55362. American Society of Mechanical Engineers, V04AT04A028.
Rentschler, M.U., Adam, F., Chainho, P., 2019. Design optimization of dynamic inter-array cable systems for floating offshore wind turbines. Renew. Sustain. Energy Rev. 111, 622–635.
Rentschler, M.U., Adam, F., Chainho, P., Krügel, K., Vicente, P.C., 2020. Parametric study of dynamic inter-array cable systems for floating offshore wind turbines. Mar. Syst. Ocean Technol. 15 (1), 16–25.
Santner, T.J., Williams, B.J., Notz, W.I., Williams, B.J., 2003. The Design and Analysis of Computer Experiments, Vol. 1. Springer.
Shields, M.D., Zhang, J., 2016. The generalization of latin hypercube sampling. Reliab. Eng. Syst. Saf. 148, 96–108.
Slot, R.M., Sørensen, J.D., Sudret, B., Svenningsen, L., Thøgersen, M.L., 2020. Surrogate model uncertainty in wind turbine reliability assessment. Renew. Energy 151, 1150–1162. http://dx.doi.org/10.1016/j.renene.2019.11.101, URL: https://www.sciencedirect.com/science/article/pii/S096014811931794X.
Sobhaniasl, M., Petrini, F., Karimirad, M., Bontempi, F., 2020. Fatigue life assessment for power cables in floating offshore wind turbines. Energies 13 (12), 3096.
Sørensen, J.D., Toft, H.S., 2010. Probabilistic design of wind turbines. Energies 3 (2), 241–257.
Spong, M.W., Hutchinson, S., Vidyasagar, M., 2006. Rigid motions and homogeneous transformations. In: Robot Modeling and Control, first ed. John Wiley & Sons, Inc., Hoboken, NJ, USA, pp. 29–53.
Stieng, L.E.S., Muskulus, M., 2020. Reliability-Based Design Optimization of Offshore Wind Turbine Support Structures Using Analytical Sensitivities and Factorized Uncertainty Modeling. Copernicus Publications.
Tarp-Johansen, N.J., 2005. Partial safety factors and characteristic values for combined extreme wind and wave load effects. J. Sol. Energy Eng. 127 (2), 242–252.
The Carbon Trust, 2020a. Floating wind joint industry project (JIP). https://www.carbontrust.com/our-projects/floating-wind-joint-industry-project. (Accessed 20 February 2021).
The Carbon Trust, 2020b. FWJIP phase II summary report. https://www.carbontrust.com/resources/floating-wind-joint-industry-project-phase-2-summary-report. (Accessed 15 February 2021).
Thies, P.R., Johanning, L., Smith, G.H., 2012. Assessing mechanical loading regimes and fatigue life of marine power cables in marine energy applications. Proc. Inst. Mech. Eng. O 226 (1), 18–32.
Toft, H.S., Svenningsen, L., Moser, W., Sørensen, J.D., Thøgersen, M.L., 2016. Assessment of wind turbine structural integrity using response surface methodology. Eng. Struct. 106, 471–483.
Vásquez, J.A.M., Avila, J.P.J., 2019. A parametric analysis of the influence of the internal slug flow on the dynamic response of flexible marine risers. Ocean Eng. 174, 169–185.
Veritas, D.N., Lloyd, G., 2010. Fatigue design of offshore steel structures. DNV Recommended Practice DNV-RP-C203.
Villaggio, P., 1997. Mathematical Models for Elastic Structures.
Vorpahl, F., Schwarze, H., Fischer, T., Seidel, M., Jonkman, J., 2013. Offshore wind turbine environment, loads, simulation, and design. Wiley Interdiscip. Rev. Energy Environ. 2 (5), 548–570.
Wang, Y., Duan, M., Gu, J., 2019. Analytical model for transfer process of deepwater steel lazy-wave riser on elastic seabed. J. Mar. Sci. Technol. 24 (1), 123–133.
Wang, L.-Z., Yuan, F., Guo, Z., Li, L.-L., 2012. Analytical prediction of pipeline behaviors in J-lay on plastic seabed. J. Waterw. Port Coast. Ocean Eng. 138 (2), 77–85.
Wilkie, D., Galasso, C., 2021. Gaussian process regression for fatigue reliability analysis of offshore wind turbines. Struct. Saf. 88, 102020.
Yang, H., Zhu, Y., Lu, Q., Zhang, J., 2015. Dynamic reliability based design optimization of the tripod sub-structure of offshore wind turbines. Renew. Energy 78, 16–25.